RSC Advances

PAPER

View Article Online
View Journal | View Issue

Cite this: *RSC Adv.*, 2023, **13**, 9998

Polydopamine-functionalized selenium nanoparticles as an efficient photoresponsive antibacterial platform†

Meng Sun,[ab] Ping Gao,[a] Bao Wang,[a] Xiangyang Li,[a] Donghan Shao,[a] Yan Xu,[a] Leijiao Li,[*ab] Yunhui Li,[*ab] Jianwei Zhu,[b] Wenliang Li[ac] and Yingxue Xue[*c]

A photoresponsive therapeutic antibacterial platform was designed and constructed using polydopamine-functionalized selenium nanoparticles as a carrier loaded with indocyanine green (Se@PDA-ICG). The therapeutic platform was confirmed by characterization and the antibacterial activity of Se@PDA-ICG against *Staphylococcus aureus* (*S. aureus*) and *Escherichia coli* (*E. coli*) was investigated. Under 808 nm laser irradiation, the antibacterial rate of Se@PDA-ICG against *E. coli* and *S. aureus* was 100% at 125 μg mL^{-1}. Furthermore, in a mouse wound infection model, the wound closure rate of the Se@PDA-ICG photoresponse group was 88.74% compared with 45.8% for the control group after 8 days of treatment, indicating that it could effectively kill bacteria and dramatically accelerate the wound healing process. These results suggested that Se@PDA-ICG could be a promising photo-activated antibacterial candidate material for biomedical applications.

Received 5th December 2022
Accepted 18th February 2023

DOI: 10.1039/d2ra07737j

rsc.li/rsc-advances

Selenium is an essential trace element for human health and has a wide range of applications in medical diagnosis.[1] Selenium nanoparticles inhibit multi-drug resistant bacteria by disrupting bacterial cell membrane integrity and are widely used to construct various therapeutic platforms.[2,3] However, the weak therapeutic function of pure selenium nanoparticles is not sufficient for clinical applications. The use of polymeric materials to functionalize nanoparticles can enhance the performance of nanomaterials.[4] Polydopamine (PDA), is a mussel-inspired material with excellent photothermal conversion properties, biocompatibility and abundant chemical reaction sites. It is often used as an interfacial chemical modifier.[5,6] In addition, indocyanine green (ICG) can kill bacteria by absorbing near-infrared light to produce reactive oxygen species (ROS) that disrupt the integrity of bacterial biofilms.[7–9] The delivery of ICG by nanoparticles could efficiently improve the chemical stability of ICG and its stability against photobleaching in various physiological environments.[10,11]

In this study, a new photoresponsive therapeutic antibacterial platform was designed and constructed using PDA-functionalized selenium nanoparticles as a carrier loaded with ICG (Se@PDA-ICG). The therapeutic platform can rapidly kill *Staphylococcus aureus* (*S. aureus*) and *Escherichia coli* (*E. coli*) with exposure to 808 nm laser irradiation, and does not easily cause pathogen resistance.[12,13] Furthermore, Se@PDA-ICG could effectively kill bacteria in bacterial infection wounds and dramatically accelerate the wound healing process. Therefore, Se@PDA-ICG is a promising light-responsive antimicrobial agent.

We first synthesized selenium nanoparticles (Se NPs) by reference to the preparation of homologous tellurium nanowires and then functionalized the surface to form a stable system using PDA (Se@PDA).[14] The PDA wrapping improves the dispersion, biocompatibility and photothermal properties of the Se NPs. Fig. 1A shows transmission electron microscopy (TEM) images of Se NPs, from which it can be seen that the Se NPs are spherical and well dispersed with a uniform size of about 90 nm (Fig. S1A†). Fig. 1B shows an X-ray diffraction (XRD) pattern of the Se NPs, matching the standard card PDF#86-2246, indicating good crystallinity and the material's relatively complete morphological structure. The X-ray photon spectra (XPS) of Se NPs show the presence of the element Se, providing evidence that the synthesized nanomaterials are Se NPs (Fig. 1C). The Se@PDA nanomaterials are shown in Fig. 1D, where a uniform transparent polymer shell layer of approximately 30 nm thickness can be observed on the surface of the Se NPs (Fig. S1B†). The Fourier transform infrared spectroscopy (FTIR) and ultraviolet-visible spectroscopy (UV-vis) spectra of Se@PDA are shown in Fig. 1E and F. The colour of the aqueous solution of Se NPs is orange, as shown in the physical illustration, and the color turns brown-black after coating with the PDA

[a]School of Chemistry and Environmental Engineering, Changchun University of Science and Technology, Changchun, 130022, China. E-mail: lileijiao@cust.edu.cn
[b]Zhongshan Institute of Changchun University of Science and Technology, Zhongshan, 528437, China
[c]Jilin Medical University, Jilin, 132013, China

† Electronic supplementary information (ESI) available. See DOI: https://doi.org/10.1039/d2ra07737j

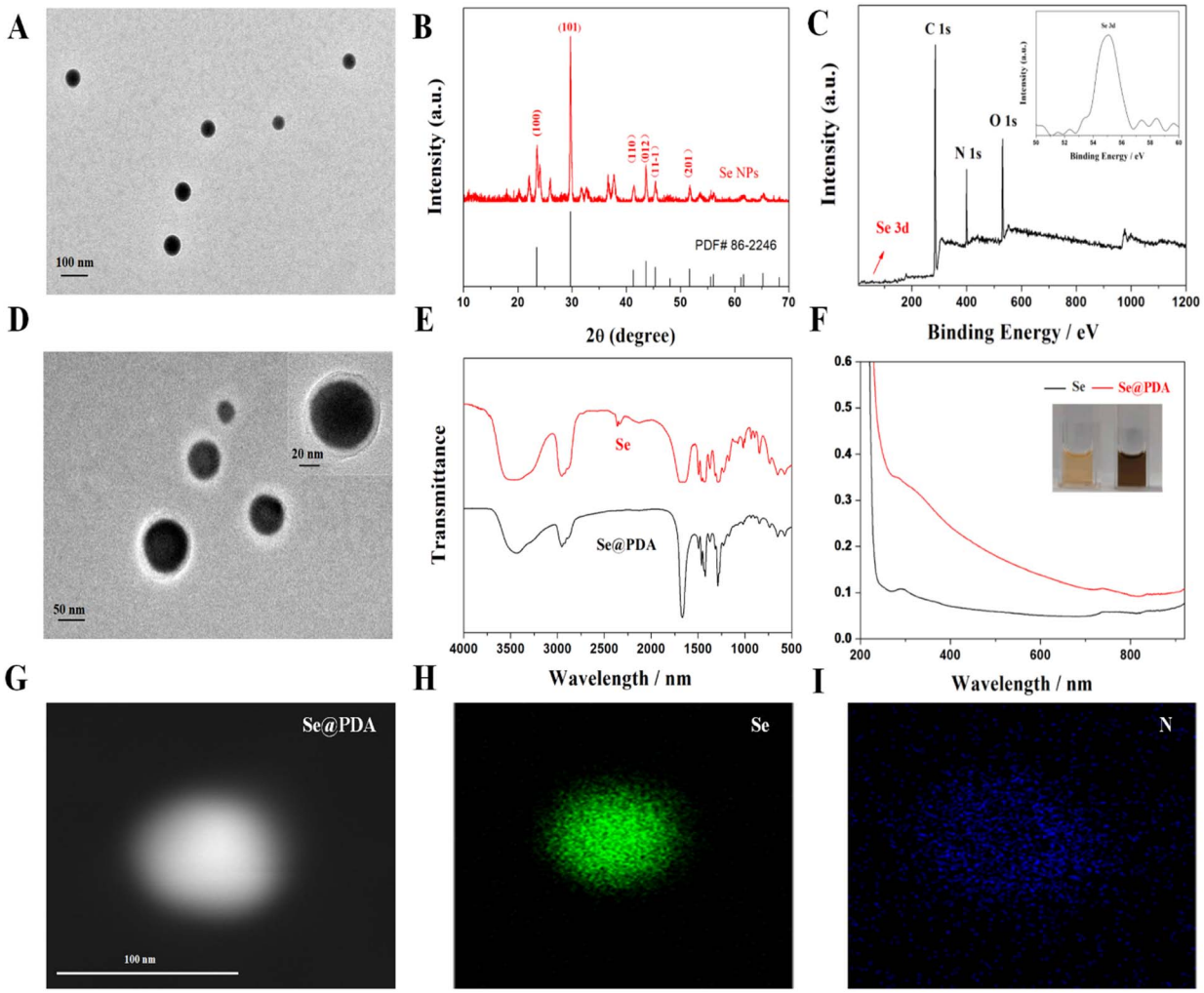

Fig. 1 Characterization of Se and Se@PDA. (A) TEM image of the Se NPs. (B) XRD pattern of the Se NPs. (C) XPS pattern of the Se NPs. (D) TEM image of Se@PDA after PDA modification. (E) FTIR spectra of Se and Se@PDA. (F) UV-vis spectra of Se and Se@PDA. (G) EDS elemental mapping of the Se@PDA sample. (H) Corresponding image of rich Se. (I) Corresponding image of rich N.

shell layer. The water and PBS solution of Se@PDA can be stable for more than 7 days (Fig. S2†). In addition, the elemental distribution of Se@PDA was characterized by elemental mapping images, which showed that Se was mainly concentrated in the nucleus of the nanoparticles, while N was mainly distributed on the outer edge of the nanoparticles to envelop Se (Fig. 1G and H).

The synthesized Se@PDA has good NIR absorption and the photothermal effect was evaluated. Aqueous solutions of Se@PDA with different concentrations of Se@PDA were placed under an NIR light source (808 nm 2 W cm^{-2}) to observe the temperature rise within 10 min. The Se@PDA group showed an excellent warming effect and a strong concentration-dependent photothermal effect compared with water (Fig. 2A). The power density of the irradiating laser had a significant effect on the photothermal property (Fig. 2B). There was no significant decrease in the warming effect after four cycles, indicating the good photothermal stability of Se@PDA (Fig. 2C). The photothermal conversion efficiency (η) of Se@PDA is 81.98% (Fig. 2D). Se@PDA has a high η compared with other similar PDA-modified materials, such as PDA/Au colloidal hollow nanoparticles (19.88%),[15] a Pt-PDA hybrid nanocomposite (44.5%)[16] and PDA-Ce6 (60.4%).[17] These results suggested that the synthesized Se@PDA have good photothermal properties.

PDA shells can be loaded with the near-infrared photosensitizer ICG through hydrophobic interaction and π–π stacking.[18] When the feeding ratio of Se@PDA and ICG was 1 : 0.8, the ICG loading rate was calculated to be 8.11% by UV absorption spectroscopy (Fig. S3 and S4†). The color of the solution changed from black-brown to dark green after loading ICG, and the average zeta potential decreased from −25 mV to −37.6 mV, further indicating the successful loading of ICG (Fig. S5†). ICG could be turned on to produce both heat and ROS under 808 nm NIR irradiation. Fig. 3A shows graphs of the photothermal warming data for Se NPs, Se@PDA and Se@PDA-ICG at a concentration of 200 μg mL^{-1} after irradiation with an 808 nm NIR laser at a power density of 2 W cm^{-2} for 10 min. More broadly, a change in the temperature of the Se NPs alone was not evident, the temperature of Se@PDA

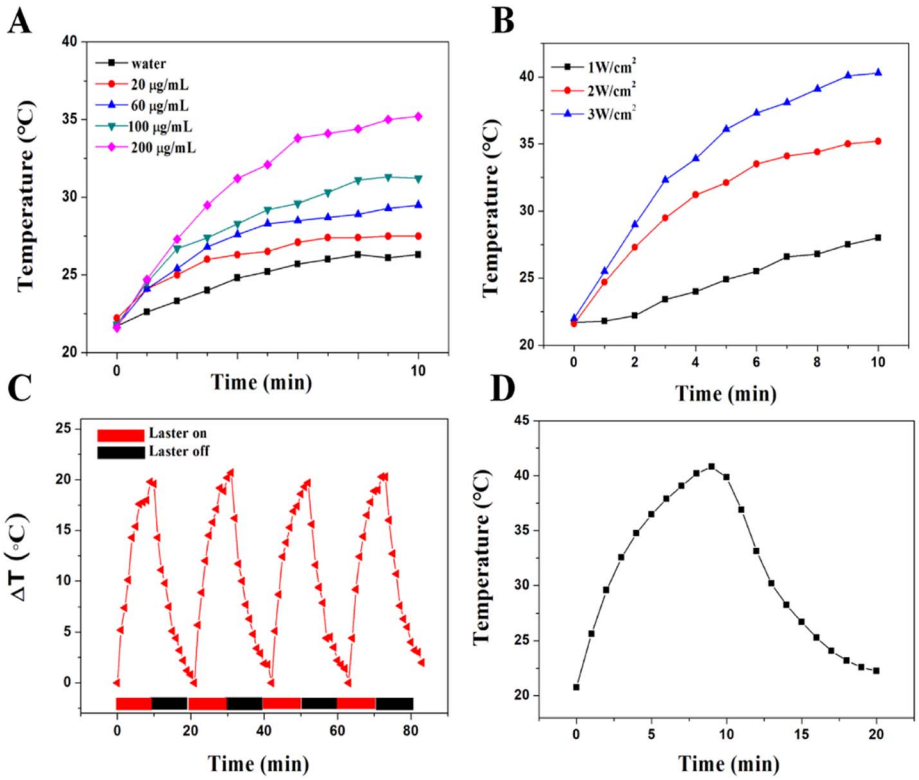

Fig. 2 Photothermal properties of Se@PDA. (A) Photothermal heating curves of different concentrations of Se@PDA (808 nm, 2.0 W cm^{-2}). (B) Temperature evolution curve of Se@PDA (200 μg mL^{-1}) solution under different NIR irradiation intensification. (C) Heating and cooling cycles at Se@PDA. (D) Cooling curve of Se@PDA.

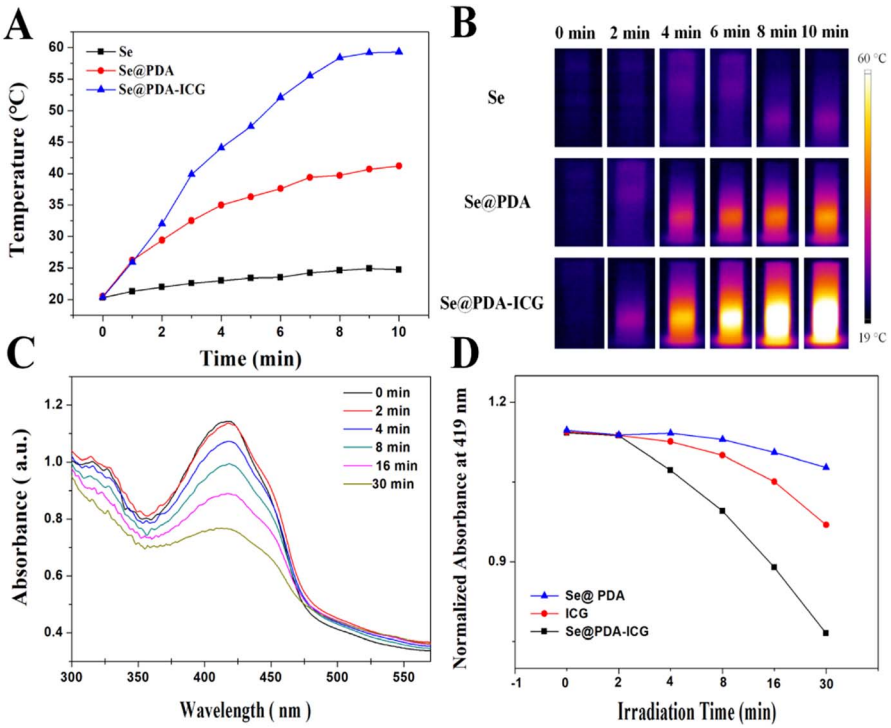

Fig. 3 The photothermal heating effect of Se@PDA-ICG and the effect of generating $^1O_2$. (A and B) Se@PDA-ICG photothermal heating curves and infrared thermal images under NIR irradiation (808 nm, 2.0 W cm^{-2}). (C) Absorption spectra of DPBF and Se@PDA-ICG at different times under 808 nm irradiation. (D) The function of absorption of DPBF at 419 nm and radiation time at 808 nm.

NPs changed slightly, while Se@PDA-ICG showed an abruptly increasing rise in temperature. The temperature of Se@PDA-ICG increased by 38.9 °C after 10 min of irradiation, exhibiting excellent warming effects at lower concentrations and power densities. The infrared thermal images of each component sample under the same conditions are presented in Fig. 3B. Obviously, the temperature of Se@PDA-ICG changed significantly with increasing irradiation time, which was in line with the temperature change curve. To assess the ability of Se@PDA-ICG to produce singly linear oxygen ($^1O_2$), DPBF was used as a fluorescent probe. DPBF can react irreversibly with $^1O_2$ and fluorescence quenching occurred, resulting in a reduction in the UV absorption peak at 419 nm. The absorbance spectrum is shown in Fig. 3C, in which Se@PDA-ICG was incubated with DPBF under 808 nm laser irradiation. The characteristic absorption peak (419 nm) of Se@PDA-ICG gradually decreased with increasing irradiation time, indicating that Se@PDA-ICG could be triggered to effectively produce $^1O_2$. Fig. 3D shows the variation in absorption at 419 nm with prolonged irradiation time of solutions containing different samples. The Se@PDA-ICG group exhibited the most effective ROS production, probably due to the more active molecular motion of ICG accompanied by the heating of Se@PDA. The above results indicated that the photothermal and photodynamic effects of Se@PDA-ICG were significantly enhanced compared to those of free ICG and Se@PDA, indicating that Se@PDA-ICG has the potential to take on the role of a photoresponsive antimicrobial therapeutic agent.

The antibacterial activity of Se@PDA-ICG was next assessed *in vitro* by plate counting with *E. coli* and *S. aureus*. PBS, Se@PDA, ICG, and Se@PDA-ICG were co-incubated with bacterial suspension for 2 h and then irradiated with the laser for 10 min (808 nm 1 W cm^{-2}). We can see in Fig. 4A and B that after the treatment of each group with *E. coli*, the survival rates of the Se@PDA, Se@PDA + NIR, ICG and ICG + NIR groups were 94.8%, 67.17%, 91.1% and 3.4%, indicating that Se@PDA and ICG can inhibit bacterial growth through photothermal and photodynamic effects, respectively. The survival rate of the Se@PDA-ICG group in the dark was 85.7%, however, that of the Se@PDA-ICG + NIR group was 0%. We could draw the conclusion that Se@PDA-ICG possessed excellent photothermal and photodynamic antibacterial effects compared with the other groups. Next, Fig. 4C and D show the bacteriostatic efficacy of each treatment group for *S. aureus*. The survival rates of the Se@PDA, Se@PDA + NIR, ICG, ICG + NIR, Se@PDA-ICG and Se@PDA-ICG + NIR groups were 96.3%, 75.8%, 90.8%, 14.9%, 47.3% and 0%, indicating an excellent sterilization effect on *S. aureus*. Compared with *E. coli*, Se@PDA-ICG was more selective for *S. aureus*. More importantly, Se@PDA-ICG showed better *in vitro* antibacterial effects than similar types of nanomaterial, such as PDA-ICG-NPs encapsulated in mixed-shell polymeric

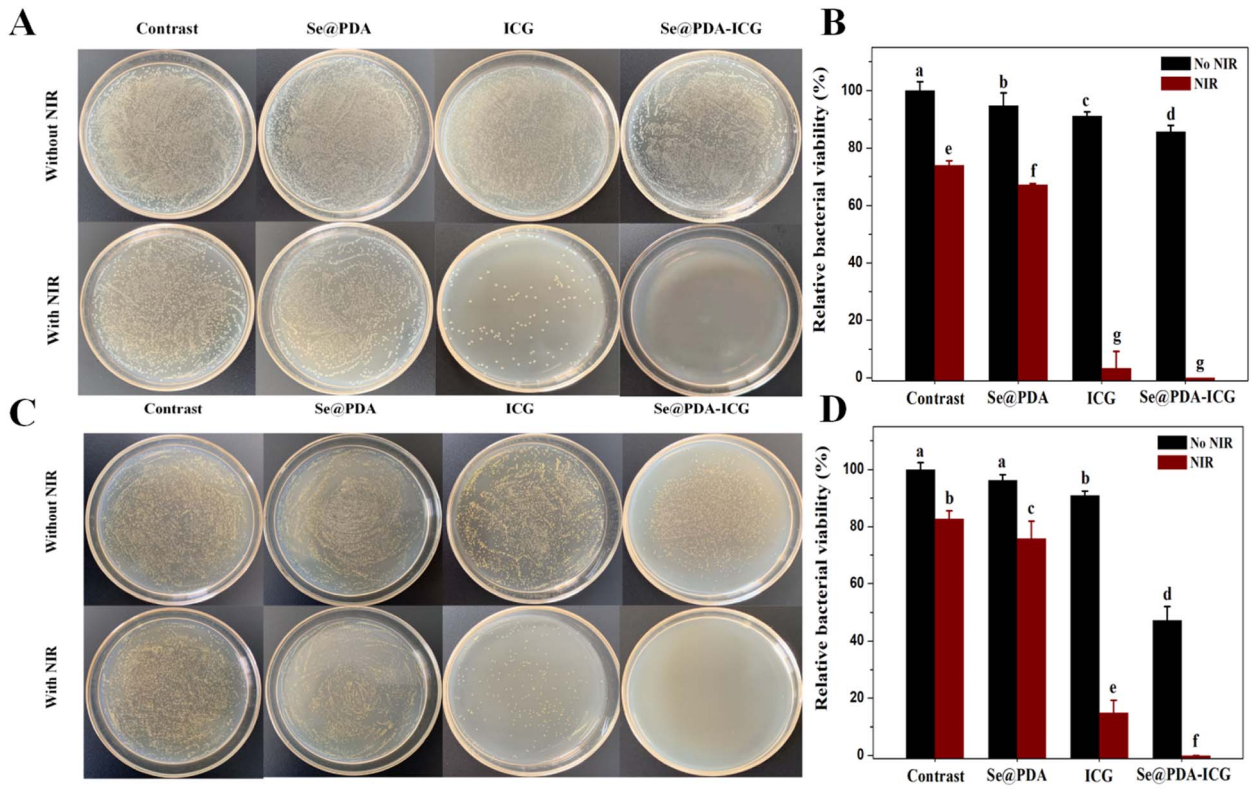

Fig. 4 *In vitro* antibacterial activity of Se@PDA-ICG. (A) *E. coli* colony photographs and data statistics of PBS, Se@PDA (125 μg mL^{-1}), ICG (10.13 μg mL^{-1}) and Se@PDA-ICG (125 μg mL^{-1}) under 808 nm laser irradiation (1.0 W cm^{-2}, 10 min). (B) The corresponding bacterial viability rates of *E. coli* ($p < 0.05$, $n = 3$). (C) Under 808 nm laser irradiation (1.0 W cm^{-2}, 10 min), *S. aureus* colony photographs and data statistics were obtained for PBS, Se@PDA (125 μg mL^{-1}), ICG (10.13 μg mL^{-1}) and Se@PDA-ICG (125 μg mL^{-1}). (D) The corresponding bacterial viability rates of *S. aureus* ($p < 0.05$, $n = 3$).

micelles.[19] The bacterial survival rate of *S. aureus* was approximately 40% after treatment with PDA-ICG-NPs under the laser for 10 min (808 nm 1.3 W cm^{-2}). The antimicrobial porous collagen scaffolds containing chitosan and Se NPs were only effective in inhibiting *S. aureus* but not *E. coli* at all.[20] Herein, Se@PDA-ICG was also more selective for *S. aureus*, which may arise from the structural differences in the bacterial outer membrane of Gram-negative and Gram-positive bacteria.[9] To further investigate the antibacterial mechanism of Se@PDA-ICG, the cell morphology of bacteria after Se@PDA-ICG treatment was observed by SEM. As can be seen in Fig. S6A and B,† the growth status of bacteria in the PBS control group was well maintained, so that the bacterial morphology was uniform and plump, while both bacterial surfaces in the Se@PDA-ICG + NIR experimental groups showed obvious wrinkling or rupture, so that the cell integrity was significantly impaired. An excellent sterilization effect from the treatment was obtained as expected. It is speculated that the antibacterial mechanism may be that Se@PDA-ICG, which is distributed near the bacterial cell wall and cell membrane, rapidly heats up and produces ROS under irradiation from a near-infrared laser. High temperature and ROS can directly damage the bacterial cell wall and membrane system, release the bacterial cytoplasmic matrix, affect its metabolism, and lead to the death of the bacteria.

Biological security is the primary requirement for further advances in the application of antibacterials. Therefore, the safety ofSe@PDA-ICG was verified by a series of experiments before *in vivo* antimicrobial assays. The effect of Se@PDA-ICG on haemoglobin was first assessed by haemolysis assays. As shown in Fig. S7A and B,† the haemolysis rate was only 0.9% even at Se@PDA-ICG concentrations up to 600 μg mL^{-1}. The cytocompatibility of Se@PDA-ICG was then determined by an MTT assay using mouse fibroblasts (L929 and NIH 3T3 cells) and the viability of both cells was above 90% when Se@PDA-ICG concentrations reached 300 μg mL^{-1} (Fig. S8†). These results indicated that the synthesized Se@PDA-ICG exhibited lower cytotoxicity and better biocompatibility than other polydopamine-modified nano-carriers of ICG. For instance, the cell survival rate was below 80% at a low concentration of 100 μg mL^{-1} for MONs@PDA-ICG (manganese oxide nanoflowers as the core), while it was also below 80% at an even lower concentration of 40 μg mL^{-1} for NDs@PDA@ICG (with nanodiamonds as the subject).[21,22] The biocompatibility of Se@PDA-ICG was further evaluated *in vivo*. The liver and kidney function and blood parameters of the mice were assessed after 7 days by tail vein injection of Se@PDA-ICG (300 μg mL^{-1} 200 μL) and the results are shown in Fig. S9.† As expected, compared with the PBS control group, the experimental group showed no significant abnormalities. The above experiments showed that Se@PDA-ICG had excellent biocompatibility and safety.

To verify the antibacterial activity of the synthesized Se@PDA-ICG *in vivo*, a wound *S. aureus* infection model was established in which PBS buffered solution was used as the control group. The wound model was created by infecting mice with *S. aureus* in a back wound and then irradiating with an NIR laser (808 1 W cm^{-2}). As can be seen in Fig. 5A, B and S10,† the results showed

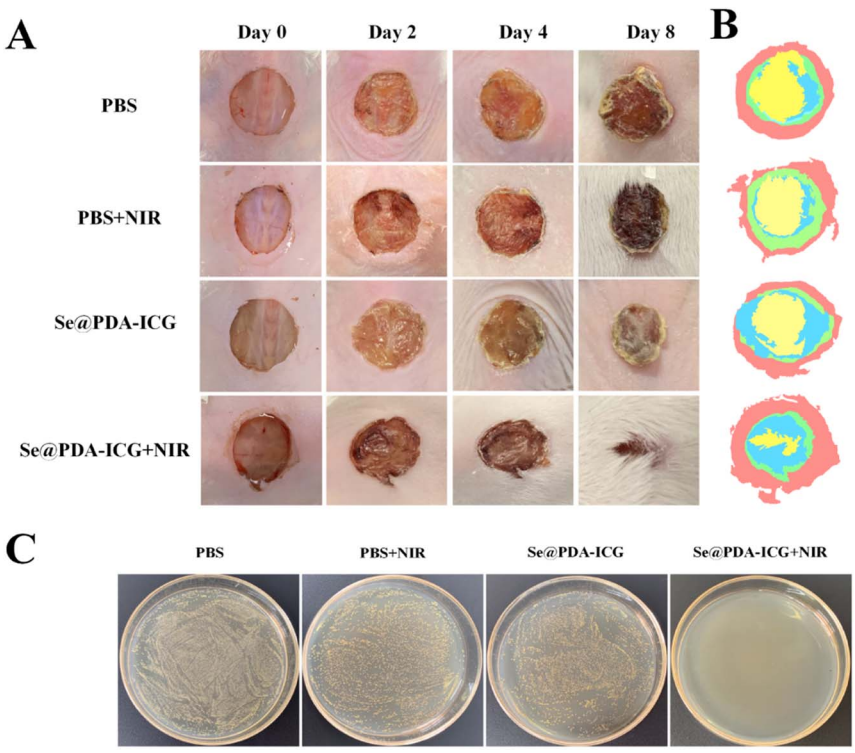

Fig. 5 *In vivo* antibacterial activity of Se@PDA-ICG under wound healing model with *S. aureus* (1.0×10^7 CFU mL^{-1}). (A) Photographs of wound healing in mice treated with PBS and Se@PDA-ICG. (B) Changes in the relative wound area of mice in different treatment groups 8 days after treatment. (C) Photographs of colonies of tissue homogenates from each group of mice 8 days after treatment.

varying degrees of reduction in trabecular area from day 0 to day 8 in all groups. 2 days after treatment, there was some yellow pus on the trabecular surface, indicating that the *S. aureus* infection model was successfully established. 8 days after treatment, the wound closure rates in the PBS, PBS + NIR, Se@PDA-ICG and Se@PDA-ICG + NIR groups were 45.8%, 55.52%, 70.36% and 88.74%, and the wound healing effect in the Se@PDA-ICG + NIR treatment group was significantly better than in the other control groups. More importantly, the Se@PDA-ICG group showed better wound closure rates than other similar light-responsive antimicrobial therapeutics on the 8th day after treatment.[23,24] Furthermore, the bactericidal effect of the different groups of wounds was assessed by plate counting on the 8th day after treatment, and the Se@PDA-ICG + NIR group had the best bactericidal effect with almost no bacteria surviving in the tissue fluid (Fig. 5C). During the treatment, the body weight of the mice remained normal with almost no significant difference between different groups (Fig. S11†), suggesting no damage to the health status of the mice.

On day 8 of wound healing, skin tissue from the trauma site was removed for pathological analysis, and the wound healing effect on each group was evaluated. Fig. S12A† shows hematoxylin and eosin (H & E) and Masson staining in each group. It can be seen from the photographs that there is still obvious inflammatory infiltration and fewer collagen fibres in the PBS group. The Se@PDA-ICG + NIR group showed intact capillaries and the greatest collagen deposition, most similar to the state of healthy tissue. In addition, the changes in cytokines during wound healing are closely related to cell metabolism and proliferation.[25] The changes in angiogenesis and inflammation in the stage of wound healing can be evaluated by double staining with VEGF and CD45. As shown in Fig. S12B,† the expression level of the VEGF factor in the Se@PDA-ICG + NIR group was the highest, and the CD45 antigen was the least. These results demonstrate that Se@PDA-ICG + NIR can promote new angiogenesis, reduce cellular inflammation and accelerate wound healing. At the end of the treatment, the stained section images of the heart, liver, spleen, lung, and kidney of the experimental groups showed no significant abnormalities compared with the control groups, indicating that the photoresponse treatment was non-invasive to the internal organs with insignificant side effects (Fig. S12C†).

In summary, the photosensitizer ICG was loaded onto PDA-functionalized Se NPs to create a photoresponsive therapeutic antibacterial platform. The Se@PDA-ICG platform can rapidly kill bacteria under 808 nm NIR irradiation. More excitingly, Se@PDA-ICG could rapidly remove infected bacteria from wounds *in vivo* and promote wound healing without toxic effects. Thus, the Se@PDA-ICG photoresponsive nanoplatform developed in this study could provide a new material or strategy for the treatment of bacterial infections.

Experimental section

Synthesis of Se NPs and Se@PDA NPs

Se NPs and PDA functionalisation were prepared from reference reports.[26,27] Typically, Na_2SeO_3 (1 mmol), weighed GSH (20 mg) and PVP (0.5 g) powder were placed in a three-necked flask and 30 mL of deionized water was poured in to dissolve them and 1 mL of NH_2OH was added as a reducing agent, then stirred magnetically for 10 min to disperse them well. After passing through an inert gas, the flask was put into a 70 °C oil bath and stirred for 1 h, centrifuged and the supernatant was retained. The supernatant was purified by dialysis and freeze–dried for 1–2 days to obtain a solid sample. An appropriate amount of Se NPs was dissolved in Tris-HCl buffer (10 mmol, pH 8.5) and a 1/4 volume of ethanol was added. The mixed system was ultrasonically dispersed for 1 h, and then dopamine hydrochloride was added. The solution was stirred for 4 h. Then the precipitation was removed by centrifugation at the end of the reaction. The supernatant was dialyzed and freeze–dried to obtain Se@PDA samples.

Photothermal effect of Se@PDA NPs

The sample solution was placed in a cuvette and irradiated at an intensity of 2 W cm^{-2} for 10 min using an 808 nm NIR laser as the excitation source, while the temperature change of the solution was recorded using a photothermal imager (Fluke PTi20). Heating–cooling curves were obtained for Se@PDA (200 μg mL^{-1}). The photothermal conversion efficiency (η) was calculated according to the relevant literature.[28,29]

Indocyanine green conjugation

The pH of an Se@PDA aqueous solution (0.5 mg mL^{-1} 2 mL) was adjusted to 2–3, then an ICG aqueous solution (0.8 mg mL^{-1} 1 mL) was added to the above system and stirred in the dark for 2 h. The dark green solution was centrifuged at 10 000 rpm for 30 minutes after the supernatant was discarded to purify it and remove the free ICG molecules. The precipitate was redispersed as a 1 mg mL^{-1} solution and stored in the dark.[30]

Bactericidal effect *in vitro*

E. coli and *S. aureus* were used to evaluate the *in vitro* bactericidal effect of Se@PDA-ICG. First, 500 μL of bacterial suspension and 500 μL of Se@PDA-ICG NPs were mixed. The bacterial suspension was 10^8 CFU mL^{-1} (OD600 0.5) and the Se@PDA-ICG concentration was 125 μg mL^{-1}. The mixture was incubated at 37 °C for 2 h and irradiated (808 nm 1.0 W cm^{-2}) for 10 min. The mixture was diluted 100 times to count the plated colonies. Se@PDA (125 μg mL^{-1}), ICG (10.13 μg mL^{-1}) and PBS were used as controls (ICG dosage was based on the loading rate).

Cytotoxicity study

Fibroblasts (L929 and NIH 3T3) were selected for the study. After the cells were cultured in good conditions, the cells were inoculated into 96-well plates and culture was continued until the cells adhered to the walls. Different concentrations of Se@PDA-ICG NPs (6.25 μg mL^{-1}, 12.5 μg mL^{-1}, 50 μg mL^{-1}, 100 μg mL^{-1}, 200 μg mL^{-1}, and 300 μg mL^{-1}) were added as the experimental group and PBS as the control group. All groups were incubated with the cells for 24 h. After incubation, MTT was added and incubation continued for 4 h. DMSO was then added and shaken

for 5 min. The absorbance at 490 nm was measured by an enzyme marker. Finally, cell viability was calculated.[31,32]

Bactericidal effect *in vivo*

Six-week-old female KM mice were purchased from Liaoning Changsheng Biotechnology Co., Ltd. and raised in SPF animal rooms. All animal procedures were performed in accordance with the Guidelines for Care and Use of Laboratory Animals of Changchun University of Science and Technology and approved by the Animal Ethics Committee of Changchun University of Science and Technology. First, the anaesthetized mice had hair removed, creating a round wound (DI 1 cm) on their back. The wound site was infected with *S. aureus* suspension (100 μL, 1.0 $\times$ 10^7 CFU mL^{-1}). 100 μL of Se@PDA-ICG solution (300 μg mL^{-1}) was added dropwise to the wounds of the experimental group and PBS as the control group, respectively. The light group was irradiated for 10 min (808 nm, 1 W cm^{-2}). The mice were returned to their cages to continue feeding after waking up. During wound healing, the wounds were measured and photographed daily to observe and record the change in wound diameter. After the treatment, the homogenates of wound tissues in each treatment group were plate counted. Skin sections were histologically analyzed by H & E, Masson, and VFGF/CD45 immunofluorescence staining.

Conflicts of interest

There are no conflicts to declare.

Acknowledgements

We greatly acknowledge the National Natural Science Foundation of China (No. 21871246), the Natural Science Foundation project of Jilin province (No. 20200201082JC), the Jilin Province Development and Reform Commission (No. 2021C039-3), and the Jilin Province Science and Technology Development Program (20190302001GX) for supporting this research.

Notes and references

1 M. P. Rayman, *Lancet*, 2000, **356**, 233–241.
2 X. Q. Huang, X. Chen, Q. C. Chen, Q. Q. Yu, D. D. Sun and J. Liu, *Acta Biomater.*, 2016, **30**, 397–407.
3 M. Sun, T. Wang, L. J. Li, X. Y. Li, Y. T. Zhai, J. T. Zhai and W. L. Li, *Front. Pharmacol.*, 2021, **12**, 702445.
4 J. X. Liu, X. L. Bao, I. Kolesnik, J. Boyan, Z. H. Yu, C. Y. Xing, J. W. Huang, T. T. Gu and X. T. Shao, *BIO Integr.*, 2022, **3**, 103–111.
5 A. Molnar, *ChemCatChem*, 2020, **12**, 2649–2689.
6 Y. Fu, L. Yang, J. H. Zhang, J. F. Hu, G. G. Duan, X. H. Liu, Y. W. Li and Z. P. Gu, *Mater. Horiz.*, 2021, **8**, 1618–1633.
7 Z. Y. Ni, J. J. Hu, Z. C. Ye, X. Wang, Y. Z. Shang and H. L. Liu, *Mol. Pharm.*, 2022, 35143213.
8 S. S. Hui, Q. Q. Liu, Y. D. Han, L. J. Zhang, J. Yang, S. Jiang, H. S. Qian and W. S. Yang, *J. Mater. Chem. B*, 2021, **9**, 9961–9970.
9 N. Topaloglu, M. Gulsoy and S. Yuksel, *Photomed. Laser Surg.*, 2013, **31**, 155–162.
10 K. Bilici, N. Atac, A. Muti, I. Baylam, O. Dogan, A. Sennaroglu, F. Can and H. Y. Acar, *Biomater. Sci.*, 2020, **8**, 4616–4625.
11 E. Gholibegloo, A. Karbasi, M. Pourhajibagher, N. Chiniforush, A. Ramazani, T. Akbari, A. Bahador and M. Khoobi, *J. Photochem. Photobiol. B*, 2018, **181**, 14–22.
12 N. Kashef, Y. Y. Huang and M. R. Hamblin, *Nanophotonics*, 2017, **6**, 853–879.
13 W. P. Taylor, P. D. Stapleton and J. P. Luzio, *Drug Discovery Today*, 2002, **7**, 1086–1091.
14 N. Yu, J. N. Li, Z. J. Wang, S. Y. Yang, Z. X. Liu, Y. S. Wang, M. F. Zhu, D. B. Wang and Z. G. Chen, *Adv. Healthcare Mater.*, 2018, **7**, 1800643.
15 B. Shang, X. F. Zhang, R. Ji, Y. B. Wang, H. Hu, B. Peng and Z. W. Deng, *Mater. Sci. Eng. C*, 2020, **106**, 110174.
16 J. H. Liang, Y. Zheng, X. W. Wu, C. P. Tan, L. N. Ji and Z. W. Mao, *Adv. Sci.*, 2020, **7**, 1901992.
17 B. Poinard, S. Z. Y. Neo, E. L. L. Yeo, H. P. S. Heng, K. G. Neoh and J. C. Y. Kah, *ACS Appl. Mater. Interfaces*, 2018, **10**, 21125–21136.
18 C. L. Hang, Z. M. Zhang, Q. Guo, L. Zhang, F. Fan, Y. Qin, H. Wang, S. Zhou, W. B. Qu-yang, H. F. Sun, *et al*, *Adv. Healthcare Mater.*, 2019, **8**, 1900840.
19 R. F. Gao, L. Z. Su, T. R. Yu, J. Liu, H. C. D. Mei, Y. J. Ren, G. J. Chen, L. Q. Shi, B. W. Busscher and H. J. Busscher, *Nanomaterials*, 2021, **11**, 3180.
20 J. Dorazilová, J. Muchová, K. Šmerková, S. Kočiová, P. Diviš, P. Kopel, R. Veselý, V. Pavliňáková, V. Adam and L. Vojtová, *Nanomaterials*, 2020, **10**, 1971.
21 Y. W. Zhu, M. Deng, N. N. Xu, Y. G. Xie and X. W. Zhang, *Front. Chem.*, 2021, **9**, 650899.
22 D. Maziukiewicz, B. Grześkowiak, E. Coy, S. Jurga and R. Mrówczyński, *Biomimetics*, 2019, **4**, 3.
23 W. W. Zhang, Z. Kuang, P. Song, W. Z. Li, L. Gui, C. C. Tang, Y. G. Tao, F. Ge and L. B. Zhu, *Nanomaterials*, 2022, **12**, 1865.
24 B. L. Liu, Y. T. Su, S. S. Wu and J. Shen, *New J. Chem.*, 2021, **45**, 18124–18130.
25 Y. T. Yang, Y. P. Liang, J. Y. Chen, X. L. Duan and . Guo, *Bioact. Mater.*, 2022, **8**, 341–345.
26 N. Yu, J. N. Li, Z. J. Wang, S. Y. Yang, Z. X. Liu, Y. S. Wang, M. F. Zhu, D. B. Wang and Z. G. Chen, *Adv. Healthcare Mater.*, 2018, **7**, 1800643.
27 Y. Y. Huang, Z. Liu, C. Q. Liu, Y. Zhang, J. S. Ren and X. D. Qu, *Chem. - Eur. J.*, 2018, **24**, 10224–10230.
28 Y. W. Zhu, M. Deng, N. N. Xu, Y. G. Xie and X. W. Zhang, *Front. Chem.*, 2021, **9**, 650899.
29 X. J. He, L. X. Dai, L. S. Ye, X. S. Sun, O. Enoch, R. D. Hu, X. G. Zan, F. Lin and J. L. Shen, *Adv. Sci.*, 2022, **9**, 2105223.
30 W. Pan, C. Liu, Y. H. Li, Y. Yang, W. L. Li, C. Feng and L. J. Li, *Bioact. Mater.*, 2022, **13**, 96–104.
31 Y. S. Jing, Z. R. Deng, X. Y. Yang, L. J. Li, Y. Gao and W. L. Li, *Chem. Commun.*, 2020, **56**, 10875–10878.
32 K. Ma, Y. W. Li, Z. G. Wang, Y. Z. Chen, X. Zhang, C. Y. Chen, H. Yu, J. Huang, Z. Y. Yang, X. F. Wang and Z. Wang, *ACS Appl. Mater. Interfaces*, 2019, **11**, 29630–29640.